Spin dynamics of YMnO₃ studied via inelastic neutron scattering and the anisotropic Hubbard model

Tapan Chatterji,[1] S. Ghosh,[2] A. Singh,[2] L. P. Regnault,[3] and M. Rheinstädter[1]

[1]*Institut Laue-Langevin, Boîte Postale 156, 38042 Grenoble Cedex, France*
[2]*Department of Physics, Indian Institute of Technology, Kanpur 208016, India*
[3]*Centre d'Etudes Nucléaires, DRFMC/SPSMS-MDN, 38054 Grenoble Cedex 9, France*

We have investigated the spin dynamics of YMnO₃ by inelastic neutron scattering and determined the spin-wave dispersion at low temperature. The spin-wave dispersions at low temperature have been analyzed with a simple nearest-neighbor anisotropic Heisenberg model and also by an anisotropic Hubbard model. Best fits are obtained only in the strong-coupling limit ($U/t > \sim 15$), with planar exchange energy $J = 4t^2/U \simeq 2.4$ meV, and anisotropy terms $D_z = U_{x'} - U_{z'} \simeq 0.32$ meV and $D_y = U_{x'} - U_{y'} \simeq 0.033$ meV. We have shown that in the strong-coupling limit, the anisotropic Hubbard model maps into the anisotropic Heisenberg model.

PACS number(s): 75.30.Ds, 75.25.+z

I. INTRODUCTION

The hole-doped LaMnO₃ compounds have induced a lot of investigations due to their colossal magnetoresistive properties.[1,2] These compounds have orthorhombic or rhombohedral near-cubic perovskitelike structure. If La is replaced by Y, Sc, and heavier lanthanides with smaller atomic radii, then a hexagonal crystal structure ($P6_3cm$) is stabilized. The hexagonal phase is stable in RMnO₃, with R =Ho, Er, Tm, Yb, Lu, Y, Sc, and also In. The Mn ions are in Mn³⁺ state with $S=2$ and are surrounded by O, forming triangular bipyramids. The hexagonal manganites are both ferroelectric and antiferromagnetic,[3–12] and the corresponding order parameters couple to each other although the ferroelectric transition temperature is as high as $T_c \sim 900$ K, whereas the Néel temperature is $T_N \sim 90$ K. This coupling between ferroelectric and magnetic order parameters yields the possibility of controlling electrical properties through magnetic field and vise versa, and therefore, hexagonal manganites may have potential applications in electronics. Due to the quasi-two-dimensional triangular lattice, the magnetic system is geometrically frustrated, which is evidenced[7] by the large ratio of Weiss-to-Néel temperatures, $\frac{\Theta}{T_N} \sim 10$. Among the rare-earth hexagonal manganites, YMnO₃ is relatively simple due to the presence of a single magnetic sublattice of Mn. It crystallizes[8] in the hexagonal space group $P6_3cm$ with lattice parameters $a = 6.1553 \pm 0.0003$ Å and c $= 11.4026 \pm 0.0008$ Å.[8] YMnO₃ orders antiferromagnetically below $T_N \approx 70$ K. The x coordinate of the Mn atoms, x $=0.315$, is very close to $1/3$, and this leads to near equality of the magnetic structure factors of pairs of possible magnetic structures with different magnetic space groups (homometry). The different possible magnetic structures of YMnO₃ are discussed in detail by Bacon.[13] Despite a few renewed neutron diffraction investigations,[8,9] the magnetic structure of YMnO₃ remained uncertain until recently. The magnetic structure of YMnO₃ has been recently investigated by three-dimensional neutron polarimetry.[14] This investigation shows that the magnetic space group of the antiferromagnetic phase of YMnO₃ is $P6_3'$. Figure 1 shows the magnetic structure of YMnO₃.

The spin-wave spectrum in a frustrated triangular antiferromagnetic system is highly interesting. Jolicoeur and Le Guillou[15] have performed spin-wave analysis of the triangular Heisenberg quantum antiferromagnet and have calculated the ground-state staggered magnetization per spin and the ground-state energy. Spin dynamics of YMnO₃ has been studied by inelastic neutron scattering on both polycrystalline sample and a single crystal by Sato *et al.*[16] They determined the spin-wave dispersions in the ordered state and fitted the data with a Heisenberg Hamiltonian by adding terms corresponding to easy-plane and in-plane easy-axis anisotropies. They observed a quasielastic central peak at the two-dimensional (2D) antiferromagnetic zone center in the Néel phase, coexisting with the conventional three-dimensional (3D) antiferromagnetic spin waves. Park *et al.*[17] have also studied the spin dynamics of YMnO₃ from polycrystalline sample and have found short-range spin correlations in the ordered phase. They found that the spin waves in YMnO₃ can be described in terms of a Heisenberg Hamiltonian with a small easy-plane anisotropy. In the present paper, we report the results of our investigation of spin excitations in YMnO₃ by inelastic neutron scattering on a single crystal. We have analyzed the spin-wave dispersion on the basis of both anisotropic Heisenberg and anisotropic Hub-
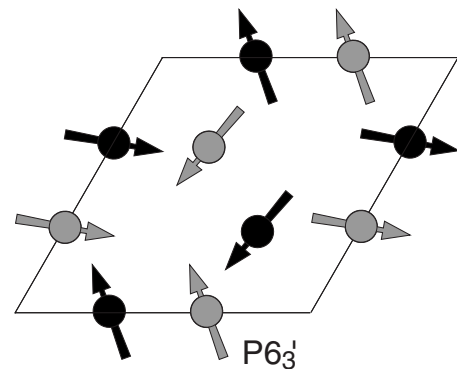

FIG. 1. Projection of the magnetic structure of YMnO₃ in the space group $P'6_3$. The black and gray circles represent Mn atoms at $z=0$ and $1/2$, respectively. Y and O atoms are omitted for clarity.

TABLE I. Crystal structure data for $YMnO_3$ obtained from the present single crystal neutron diffraction experiment. Space group $P6_3cm$, $a=6.132(1)$ Å and $c=11.452(8)$ Å (at $T=70$ K).

Atom		Position	x^a	y^a	z^a
Mn	6(c)	$x,0,z$	0.315(2)	0	0
Y1	2(a)	$0,0,z$	0	0	0.265(3)
Y2	4(b)	$1/3,2/3,z$	0.3333	0.6667	0.217(4)
O1	4(c)	$x,0,z$	0.3118(14)	0	0.155(4)
O2	4(c)	$x,0,z$	0.637(3)	0	0.329(2)
O3	2(a)	$0,0,z$	0	0	0.462(4)
O4	4(b)	$1/3,2/3,z$	0.3333	0.6667	0.010(3)

^{a}Values obtained at $T=100$ K.

bard models. In both these models, the anisotropy has been introduced only phenomenologically. We have shown that in strong-coupling limit, the anisotropic Hubbard model maps into an anisotropic Heisenberg model.

We have organized the paper in the following way: In Sec. II, we describe the experimental procedure. In Sec. III, we describe the results of neutron diffraction investigation of the crystal structure, magnetic phase transition, and magnetic diffuse scattering close to the Néel temperature $T_N \approx 70$ K. In Sec. IV, we describe the results of inelastic neutron scattering investigation of the spin-wave dispersion of $YMnO_3$ at low temperature. In Sec. V, we describe the results of the temperature dependence of the spin-wave energy. In Sec. VI, we analyze the spin-wave dispersion with an anisotropic Heisenberg model. In Sec. VII, we analyze the spin-wave dispersion with an anisotropic Hubbard model. In Sec. VIII, we summarize the results of the present investigation and draw some conclusions.

II. EXPERIMENTAL PROCEDURES

Neutron diffraction measurements were performed on an $YMnO_3$ single crystal on the diffractometer D10 of the Institut Laue-Langevin. We performed inelastic neutron-scattering experiments on the same $YMnO_3$ single crystal by using the thermal triple-axis spectrometers IN22 and IN20. To investigate the lower energy part of the dispersion, we also performed experiments on the cold three-axis spectrometer IN12. All these instruments, except for IN20, are located at the guide hall of the Institute Laue-Langevin in Grenoble and have very low background. The same $YMnO_3$ single crystal of size $4 \times 5 \times 4$ mm^3 has been used for all above-mentioned investigations. To obtain low temperatures, the crystal was placed inside a conventional ^{4}He Orange-type cryostat.

III. NEUTRON DIFFRACTION INVESTIGATION

To test the quality of the single crystal and to characterize the low-temperature magnetic properties, we did single crystal neutron diffraction measurements on $YMnO_3$ on diffractometer D10. The purpose of this investigation was to check whether the present crystal has the same crystal structure and
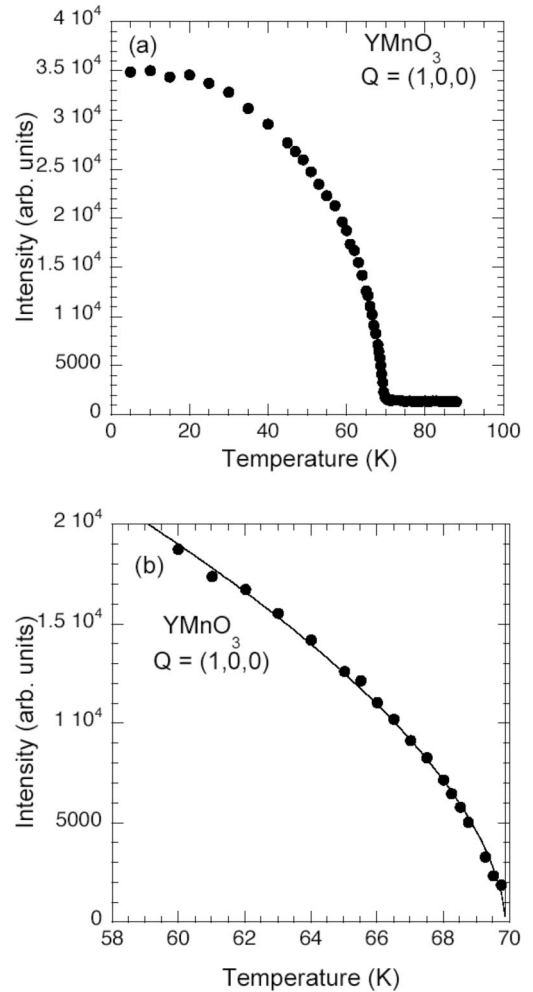

FIG. 2. (a) Temperature variation of the 100 reflection and (b) the fit of the intensity data close to T_N for the determination of the critical exponent given by Eq. (1).

shows similar magnetic properties already reported in the literature.[4,5,8] The sample rotation scans of the Bragg peaks showed that the widths of the diffraction peaks are resolution limited. The lattice parameters and orientation matrix were determined from the angles of a set of centered Bragg peaks at $T=70$ K. The refined lattice parameters at $T=70$ K were $a=6.132\pm0.001$ Å and $c=11.452\pm0.008$ Å. However, the absolute values of lattice parameters obtained by single crystal neutron diffraction data are affected by systematic errors due to the difficulty of centering a relatively large single crystal and also due to the error in the value of the neutron wavelength used. The integrated intensities of 350 reflections from $YMnO_3$ with $\sin\theta/\lambda < 0.38$ Å^{-1} were measured at a wavelength of 2.26 Å at $T=5$ K and also at $T=100$ K, in the magnetic ordered and paramagnetic states, respectively. The intensities of equivalent reflections were averaged together. The final 100 and 5 K data sets contained respectively 45 and 61 independent reflections. We refined the crystal structure of $YMnO_3$ by using the neutron diffraction data at $T=100$ K. Table I gives the refined structural parameters. We also refined the magnetic structures with the neutron diffraction data collected at $T=5$ K. The intensity data alone give
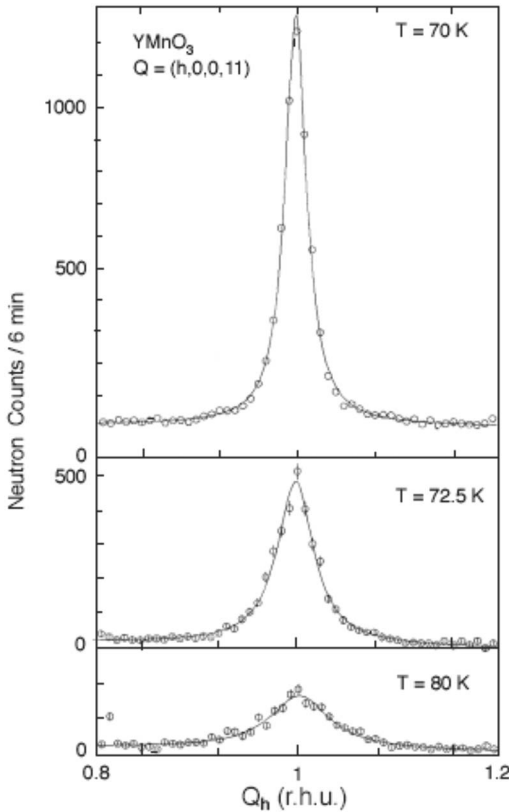
FIG. 3. Q scans parallel to a^* at $Q=(1,0,0.11)$. The scans are perpendicular to the rodlike diffuse magnetic intensity of the quasi-two-dimensional YMnO₃.
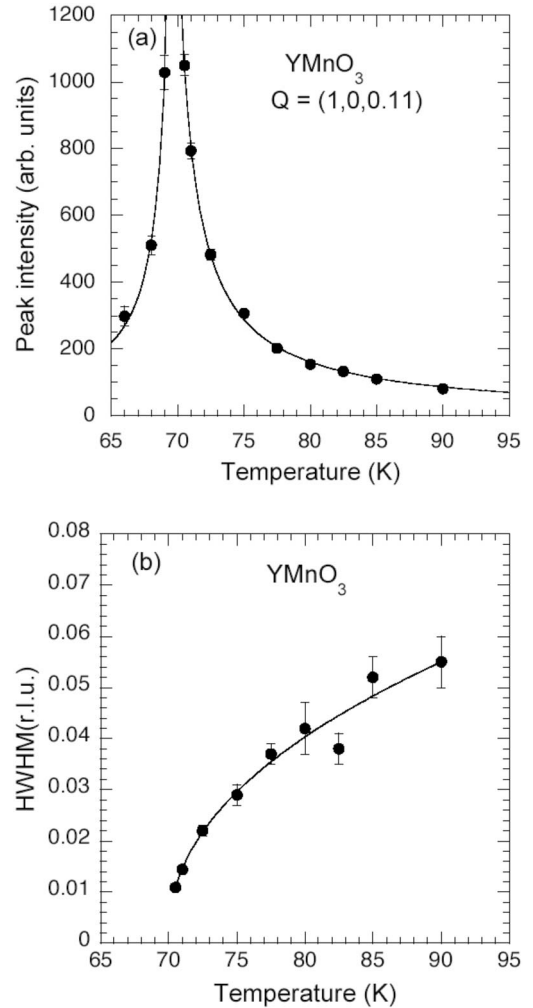

FIG. 4. (a) Temperature dependence of the peak intensity of the diffuse scattering maximum at $Q=(1,0,0.11)$ obtained in a scan perpendicular to the rod direction shown in Fig. 3. The intensity is proportional to the susceptibility. The continuous curve for $T>T_N$ is the result of the power law fit of the data with Eq. (2). (b) Temperature variation of the half-width at half-maximum (HWHM) of YMnO₃ obtained from the scans shown in Fig. 3. The HWHM is proportional to the inverse correlation length. The continuous line is the power law fit with Eq. (3).

equally good fits to all the possible nearly homometric magnetic structure models discussed by Bacon,[13] and cannot distinguish between these models. We already noted that the magnetic structure of YMnO₃ has been solved recently by three-dimensional neutron polarimetry.[14]

In order to determine the Néel temperature and magnetic correlations above T_N, we investigated the temperature of the magnetic reflections of YMnO₃. Figure 2(a) shows the temperature variation of the integrated intensity of the 100 reflection from YMnO₃ measured on D10. The intensity of this reflection decreases continuously and becomes constant above $T_N \approx 70$ K. The temperature independent intensity above T_N is due to the structural contribution to the intensity. We have fitted the temperature dependence of intensity close to T_N by the equation

$$I = I_n + I_0 \left(\frac{T_N - T}{T_N} \right)^{2\beta}, \qquad (1)$$

where I is the integrated intensity of the 100 reflection and I_n is the nuclear (structural) contribution to the intensity. The least squares fit gave $T_N=69.89\pm0.05$ K and $\beta=0.295\pm0.008$. The obtained value of β is close to that expected for a 3D XY or Ising system.[18] Figure 2(b) shows the resultant fit. We must note that β determined by the present investigation cannot really be identified with the critical exponent. In order to determine the critical exponent β, one should not refine T_N from the temperature dependence of the

intensity of the magnetic Bragg peak, but it should be independently determined from the divergence of the diffuse intensity at the ordering temperature.[18,19] Also a possible temperature variation of the extinction parameters may hinder the determination of the critical exponent.[19] We have not attempted such rigorous investigation of the critical exponent β. The exponent β of YMnO₃ determined by Roessli et al.[20] is $\beta=0.187\pm0.002$, much lower than the value obtained by us. However, Roessli et al. have fitted the intensity data belonging to a noncritical range of temperatures and, hence, cannot be identified with the critical exponent.

YMnO₃ is a quasi-2D magnetic system. So one expects diffuse scattering rods parallel to c^* close to $T_N \approx 70$ K. We have, indeed, found such rod scattering above T_N, in agreement with the results of Lonkai et al.[21] We performed several Q scans perpendicular to the rod across $Q=(1,0,0.11)$. Fig-
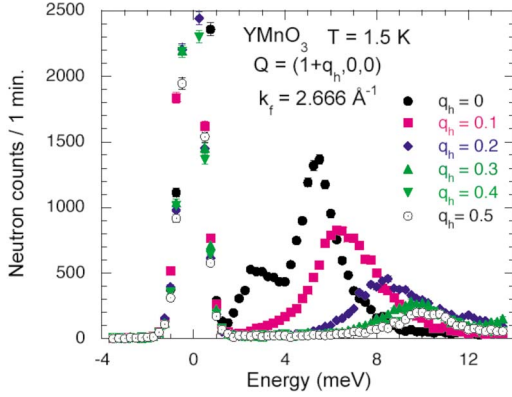
FIG. 5. (Color online) Energy scans of YMnO$_3$ at $Q=(1+q_h,0,0)$ for several q_h values, measured with the thermal triple-axis spectrometer IN22.

FIG. 6. (Color online) Energy scans of YMnO$_3$ at $Q=[1,0,0+q_l]$ for several q_l values, measured with the thermal triple-axis spectrometer IN22.

ure 3 shows such Q scans parallel to a^* perpendicular to the rod. We fitted a Lorentzian function convoluted with the Gaussian resolution function of the instrument measured from the 100 Bragg peak. Figure 4(a) shows the temperature variation of the peak intensity of the diffuse scattering maximum at $Q=(1,0,0.11)$, obtained in a scan perpendicular to the rod direction. The peak intensity is proportional to the susceptibility $\chi(T)$. The data for $T>T_N$ have been fitted by the power law

$$\chi(T) = A\left(\frac{T-T_N}{T_N}\right)^{-\gamma}, \qquad (2)$$

giving $\gamma=0.97\pm0.05$ and $T_N=68.9\pm0.2$. The value of fitted γ agrees with the mean-field value $\gamma=1$ within experimental error. The data for $T<T_N$ could, in principle, be fitted similarly, but have not been done because of the lack of enough number of data points. The continuous curve for $T<T_N$ is a guide for the eye. The half-width at half-maximum (HWHM) of the fitted curve gives the inverse in-plane correlation length κ. Figure 4(b) shows the temperature dependence of the inverse correlation length. The continuous line is the fit with the equation

$$\kappa(T) = A\left(\frac{T-T_N}{T_N}\right)^{\nu}. \qquad (3)$$

The fit gave $T_N=70.0\pm0.5$ and $\nu=0.45\pm0.08$, which is close to the mean-field value $\nu=\frac{1}{2}$ but far from the value $\nu\approx\frac{2}{3}$ expected for an XY or Heisenberg systems.[18] Roessli *et al.*[20] determined the critical exponent ν in YMnO$_3$ to be $\nu=0.57\pm0.06$. This value is somewhat larger than the value obtained by us. Roessli *et al.*[20] studied the spin fluctuations in YMnO$_3$ above T_N in detail using both unpolarized and polarized inelastic neutron scattering. They found an in-plane and an out-of-plane excitation. The in-plane mode has two components just above T_N, a resolution-limited central peak and a quasielastic component with a linewidth that increases as a function of momentum transfer. The out-of-plane fluctuations are inelastic at the magnetic zone center and do not show any q dependence for small wave vectors.
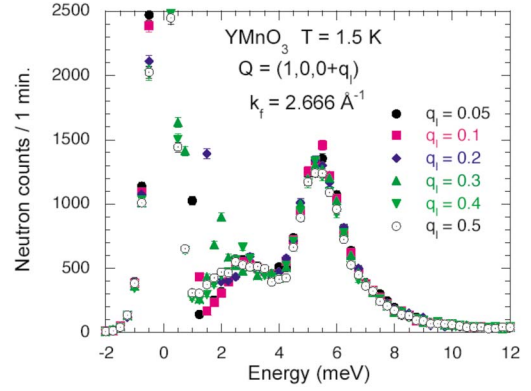
We must add that the study of the critical exponents in YMnO$_3$ is still at the very initial state and will be continued in the future. Also it is not clear whether the present frustrated quasi-2D magnetic system has a completely different universality class or not.

IV. SPIN DYNAMICS AT LOW TEMPERATURE

We performed both constant-energy and constant-Q scans from YMnO$_3$ around $Q=(1,0,0)$ on the thermal three-axis spectrometer (TAS) IN22. Figure 5 shows some constant-Q scans at $Q=(1+q_h,0,0)$ for several q_h. These constant-Q scans were limited to the energy transfer of about 13 meV and did not cover the higher energy modes. Figure 6 shows energy scans of YMnO$_3$ at $Q=(1,0,0+q_l)$ for several q_l. To extend the energy range covered and to determine the dispersion of the third spin-wave branch expected in a triangular magnetic structure, we did in a subsequent experiment on TAS IN20 the constant-Q scans at $Q=(1+q_h,0,0)$ and also at $Q=(q_h,0,3)$, shown in Figs. 7 and 8, respectively. Also to determine more precisely the spin-wave dispersion corresponding to small energy transfer and especially to study the
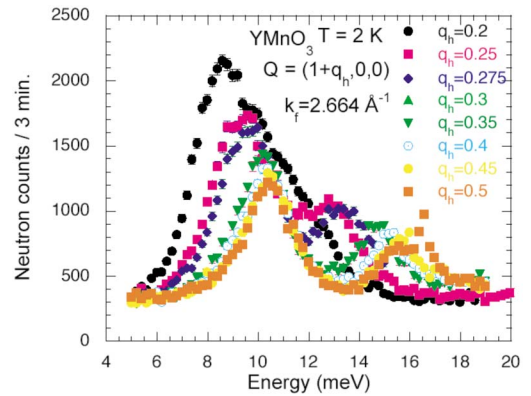

FIG. 7. (Color online) Energy scans of YMnO$_3$ at $Q=(1+q_h,0,0)$ for several q_h values, measured with the thermal triple-axis spectrometer IN20.
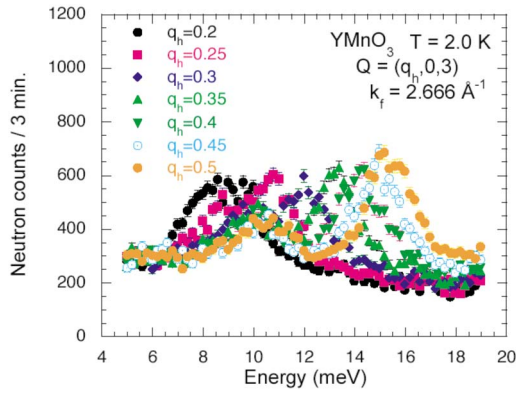
FIG. 8. (Color online) Energy scans of YMnO$_3$ at Q =(q_h,0,3) for several q_h values, measured with the thermal triple-axis spectrometer IN20.

FIG. 10. (Color online) Spin-wave dispersion of YMnO$_3$ at T =1.5 K along [100]. The dotted curves are model calculations based on a nearest-neighbor anisotropic Heisenberg model.

dispersion along [001], we did scans on the cold triple-axis spectrometer IN12. Figure 9 shows the constant-Q scans of YMnO$_3$ at Q=[1,0,q_l] for several q_l values measured with the cold triple-axis spectrometer IN12. The inelastic peaks could be fitted with Gaussian functions to give the energies of spin-wave excitations.

Figure 10 shows the dispersion of spin waves in YMnO$_3$ along [100], determined from the constant-Q scans on the thermal three-axis spectrometers IN22 and IN20 as on well as the cold three-axis spectrometer IN12. A few constant-energy scans were also performed as mentioned before. We observe two spin-wave branches in the constant-Q scans at Q=(1+q,0,0). These two branches have energies of about 2.4 and 5.3 meV at the magnetic zone center. These two branches approach each other at q_h=0.1 r.l.u. and ΔE =6.5 meV. For higher q_h, the energy of these two branches increases continuously, showing maximum values of about 10 and 16 meV, respectively, at the zone boundary. The total spin-wave bandwidth is only about 12.5 meV. The energy widths of the spin-wave branches are much larger than the instrumental resolution, showing that the spin waves in
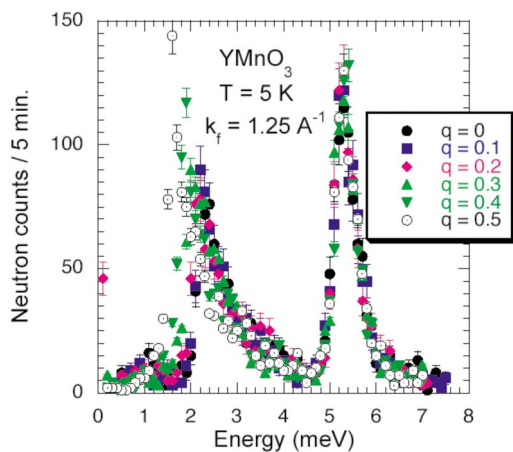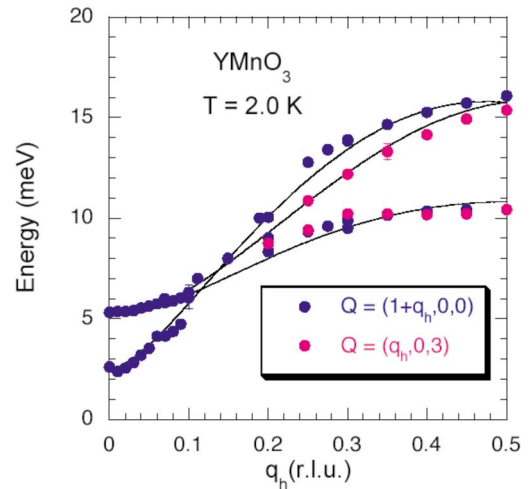
YMnO$_3$ are damped even at low temperature. In a subsequent experiment on IN20, we measured the dispersion of the third spin-wave branch expected in a triangular magnetic structure in constant-Q scans performed at Q=(q_h,0,3). This branch was not observed at Q=(1+q,o,o) because of the structure factor. It should be noted that the dispersion of the third branch can be determined from the parameters determined from dispersions of the first and second branches only. In fact, we calculated it before measuring it actually. This is also clear from the results of the analysis of the spin-wave dispersion by the anisotropic Heisenberg and anisotropic Hubbard models described in the subsequent section.

The spin-wave dispersion along [001] is very small as evidenced by Fig. 6 and could not be determined precisely from the measurements on a thermal triple-axis spectrometer like IN22. We, therefore, did additional measurements on the cold triple-axis spectrometer IN12. Figure 11 shows the spin-wave dispersion of YMnO$_3$ at T=5 K along [001] measured with IN12. The relatively small dispersions along [001] show that YMnO$_3$ is a quasi-2D magnetic system.

The spin-wave dispersion determined by us does not quite agree with those determined by Sato *et al.*[16] We see a clear third branch in our constant-Q scans at Q=(q_h,0,3) and this branch is well separated from the branch determined by the constant-Q scans at Q=(1+q_h,0,0). Sato *et al.*[16] really determined only two branches for q_h>0.2. The statistics of the present scans is far superior than that reported by Sato *et al.*[16] Sato *et al.*[16] claims to have seen a Goldstone-like mode although they did not plot any data point supporting this claim. Our model calculations and also our extensive scans close to the zone center do not support the existence of any Goldstone-like mode. Also Sato *et al.*[16] used the wrong magnetic structure model for the calculation of spin-wave dispersion. The correct magnetic structure determined from spherical neutron polarimetry[14] was not then available to them.

FIG. 9. (Color online) Energy scans of YMnO$_3$ at Q=(1,0,0 +q_l) for several q_l values, measured with the cold triple-axis spectrometer IN12.
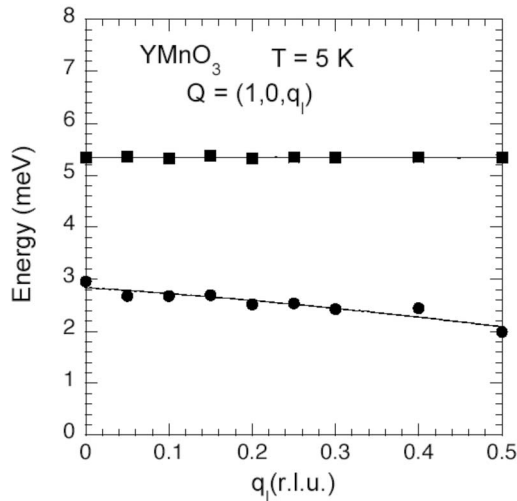
FIG. 11. Spin-wave dispersion of YMnO$_3$ at $T=5$ K along [001]. The small dispersions along [001] shows that YMnO$_3$ is a quasi-two-dimensional magnetic system. The continuous lines are guides for the eye.

V. TEMPERATURE DEPENDENCE OF THE SPIN DYNAMICS

We have measured the temperature dependence of the energy of the spin-wave mode at $Q=(1,0,0)$, at $Q=(1.1,0,0)$, and also at $Q=(1,0,0.5)$. Figure 12 shows the temperature dependence of the energy of the inelastic peak at $Q=(1.1,0,0)$ of YMnO$_3$. The energy decreases from $E=6.8$ meV at $T=1.7$ K with increasing temperature and becomes $E=1.3$ meV at $T_N \approx 70$ K. We note that the energy of the spin waves remains finite at T_N and also at temperatures up to about 10 K above T_N. Figure 13 shows some of the constant-Q scans at $Q=[1,0,0]$ at different temperatures. The two peaks observed in these scans correspond to the two spin-wave gap energies. The energies of the two observed spin-wave branches decrease continuously as a function of
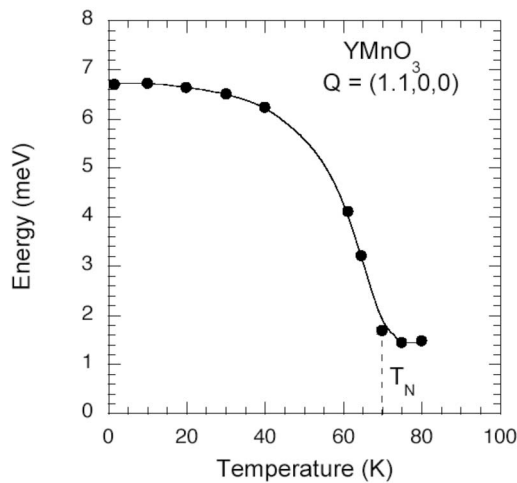

FIG. 12. Temperature variation of the energy of the inelastic peak at $Q=(1.1,0,0)$ of YMnO$_3$. The continuous curve is a guide for the eye.
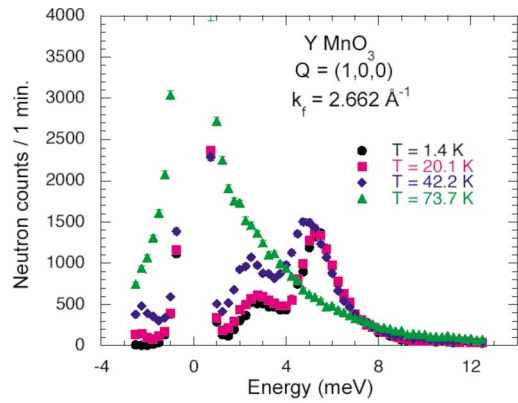

FIG. 13. (Color online) Energy scans of YMnO$_3$ at $Q=[1,0,0]$ at several temperatures.

temperature as expected. At temperatures above $T_N \approx 70$ K, the two-peak structure is lost, but a substantial scattering is observed on the positive energy side. Figure 14 shows some of these scans at $Q=[1,0,0]$ at different temperatures. Figure 15 shows the temperature dependence of the spin-wave energies measured at $Q=[1,0,0.5]$. The spin-wave energies decrease with temperature, but do not become zero at $T_N \approx 70$ K. We have investigated spin-wave excitations in YMnO$_3$ above T_N in more details by using a multianalyzer detector. The results[22] of this investigations will be published elsewhere.

VI. HEISENBERG MODEL ANALYSIS OF THE SPIN-WAVE DISPERSION

It turned out that the spin-wave dispersion in YMnO$_3$ in the *a-b* plane can be analyzed approximately by a Heisenberg Hamiltonian including in-plane and out-of-plane anisotropic terms. Sato *et al.*[16] have employed a similar model, but have included two in-plane and two interplane interactions. We, however, prefer to start with only nearest-neighbor in-plane interaction for describing the measured spin-wave dispersion along q_h. One can, thus, introduce the following model spin Hamiltonian:
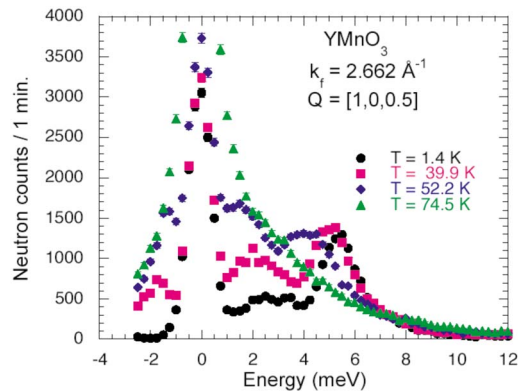

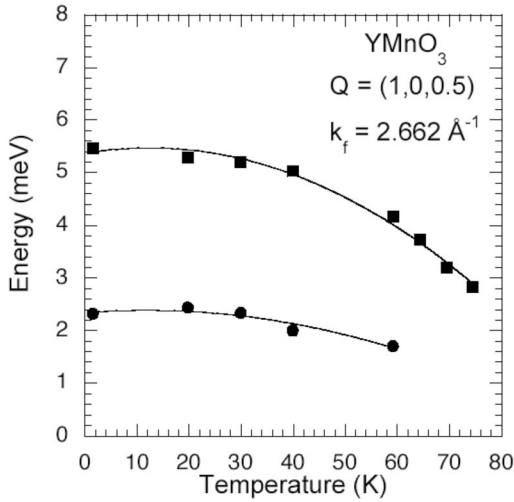FIG. 14. (Color online) Energy scans of YMnO$_3$ at $Q=[1,0,0.5]$ at several temperatures.

FIG. 15. Temperature dependence of the spin-wave energies measured at $Q=[1,0,0.5]$. The continuous lines are guides for the eye.

$$H = J\sum_{\langle ij \rangle} \mathbf{S_i} \cdot \mathbf{S_j} + D_y \sum_i (S_i^y)^2 + D_z \sum_i (S_i^z)^2, \quad (4)$$

where $\langle i,j \rangle$ indicates that the sum is over nearest-neighbor in-plane pairs, J is the primary antiferromagnetic exchange, and D_y and D_z are the anisotropy constants. The spin directions in Eq. (4) correspond to the locally-rotated spin coordinate system, as described below in Eq. (12). A somewhat similar model has been used by Vajk et al.,[23] who have included only one anisotropy. Introducing three different flavors of bosons and using a Holstein-Primakoff transformation, one can derive a linearized Hamiltonian that can be diagonalized by mapping to the Hamiltonian of the quadratic quantum mechanical oscillator. The lattice Fourier sum z is defined as

$$z = \frac{1}{12}[e^{-2\pi i(h/3-k/3)} + e^{2\pi i(2h/3+k/3)} + e^{-2\pi i(h/3+2k/3)}]. \quad (5)$$

Introducing

$$z_1 = z + z^*,$$

$$z_2 = -(z+z^*)/2 + i(\sqrt{3}/2)(z-z^*),$$

$$z_3 = -(z+z^*)/2 - i(\sqrt{3}/2)(z-z^*), \quad (6)$$

where z^* is the complex conjugate of z, we can express the dispersion of the three modes $\hbar\omega_i$ by

$$\hbar\omega_i = 3JS\sqrt{[(1+4z_i+2D_z/3J)(1-2z_i+2D_y/3J)]}, \quad (7)$$

where $i=1,2,3$, and $S=2$ for Mn^{3+} ion. Equation (7) can also be obtained in the "strong-coupling" limit of the anisotropic Hubbard model discussed in the next section. Figure 10 shows the calculated dispersions by using the three parameters $J=2.4$ meV, $D_z=0.31$ meV, and $D_y=0.036$ meV. The exchange interaction parameter and the anisotropy constants obtained are close to those obtained from the fit with the Hubbard model described in the next section. The agreement

is quite reasonable, noting that the Hubbard model is mapped into the Heisenberg model in the strong-coupling limit.

We note that the present simple nearest-neighbor anisotropic Heisenberg model used by us rationalizes all observed experimental facts. On the contrary, the model used by Sato et al.[16] is unnecessarily complex and predicts four modes not observed experimentally. The clear existence of two spin-wave gaps implies that there should be no Goldstone modes. In the three-sublattice hexagonal system, one expects either three modes or, in the case of more complex structure, six modes but never four. Sato et al.[16] have neither given any analytical formula for the spin-wave dispersion nor indicated how they would calculate the spin-wave dispersion in case the calculations were done numerically.

VII. SPIN-WAVE DISPERSION WITHIN THE ANISOTROPIC HUBBARD MODEL

It has been shown recently that the neutron-scattering data[23] for spin-wave dispersion in HoMnO$_3$ are well described by an anisotropic Hubbard model on a triangular lattice with an easy-plane anisotropy. Best fit indicated that magnetic excitations in HoMnO$_3$ correspond to the strong-coupling limit $U/t > \sim 15$, with planar exchange energy $J = 4t^2/U \simeq 2.5$ meV and planar anisotropy $\Delta U \simeq 0.35$ meV.[24]

Spin-wave excitations in the 120° antiferromagnetic (AF) state of the Hubbard model on a triangular lattice have been studied earlier in the full U range.[25] The spin-wave energy, evaluated in the random phase approximation (RPA), was found to asymptotically approach the quantum Heisenberg antiferromagnet result in the large U limit, thus providing a continuous interpolation between weak- and strong-coupling limits. However, finite-U-induced competing interactions and frustration were found to significantly modify the dispersion, resulting in vanishing spin stiffness at $U \approx 6$ and a magnetic instability at $U \approx 7$, corresponding to vanishing spin-wave energy at wave vector $\mathbf{q}_M = (\frac{\pi}{3}, \frac{\pi}{\sqrt{3}})$. The sharp falloff of ω_M near $U \approx 7$ provides a sensitive indicator of finite-U effects in the AF state. Indeed, recent high-resolution neutron-scattering studies of the spin-wave dispersion in the square lattice $S=1/2$ AF La$_2$CuO$_4$ have revealed noticeable spin-wave dispersion along the magnetic Brillouin zone (MBZ) edge,[26] associated with finite-U double-occupancy effects.[27]

In this section, we calculate the spin-wave dispersion by including easy-plane and in-plane easy-axis anisotropies, and show that the neutron-scattering data for YMnO$_3$ are similarly well described by a Hubbard model on a triangular lattice, thus providing a microscopic description of the most essential features of spin dynamics, including the spin-wave dispersion and the energy scale.

The Mn spin anisotropies are, however, treated here only at a phenomenological level, equivalent to the effective anisotropy $D_1 S_{iz}^2$ and $D_2(\mathbf{S}_i \cdot \mathbf{n}_i)^2$ included in recent investigations using spin models.[16,23] In a detailed study of single-ion anisotropy and crystal-field effects in the layered rare-earth cuprates R_2CuO$_4$ (R=Nd, Pr, and Sm), the magnetic behavior (including spin-reorientation transitions) has been attributed to coupling of Cu with the rare-earth magnetic subsystem which exhibits a large single-ion anisotropy, resulting

in preferential ordering of rare-earth moments along specific lattice directions.[28] It has been suggested that the anisotropy of Mn spins, its observed temperature dependence, and the reorientation transitions in HoMnO$_3$ also originate from a similar anisotropic exchange coupling with the rare-earth holmium,[23] resulting in magnetic behavior as seen in layered rare-earth cuprates, where frustrated interlayer coupling allows for weaker, higher-order interactions to control the magnetic structure. Presumably, a similar origin can be attributed to all the corresponding phenomena in YMnO$_3$ as well. Especially relevant for noncollinear ordering, the anisotropic exchange (Dzyaloshinski-Moriya) interaction $\mathbf{D} \cdot (\mathbf{S}_i \times \mathbf{S}_j)$ originating from spin-orbit coupling has been suggested as responsible for the clamping of ferroelectric and antiferromagnetic order parameters in YMnO$_3$.[29]

Hund's rule coupling responsible for the $S=2$ spin state of Mn^{+++} ions and crystal-field splitting have also not been realistically incorporated here. However, these realistic details do not qualitatively affect the spin-rotation symmetry and spin dynamics, as discussed below. Hund's rule coupling in the generalized Hubbard model considered here is maximal as interorbital Coulomb interaction for parallel spins is dropped completely. Including an interorbital density-density interaction V_0 and an intra-atomic exchange interaction F_0 favoring parallel-spin alignment (Hund's rule coupling), the more realistic orbital Hubbard model[30,31]

$$H = -t \sum_{i,\delta,\gamma,\sigma} a^\dagger_{i\gamma\sigma} a_{i+\delta,\gamma\sigma} + U \sum_{i\gamma} n_{i\gamma\uparrow} n_{i\gamma\downarrow}$$
$$+ \sum_{i,\gamma<\gamma',\sigma,\sigma'} (V_0 - \delta_{\sigma\sigma'} F_0) n_{i\gamma\sigma} n_{i\gamma'\sigma'}$$
$$+ F_0 \sum_{i,\gamma<\gamma',\sigma\neq\sigma'} a^\dagger_{i\gamma\sigma} a_{i\gamma'\sigma} a^\dagger_{i\gamma'\sigma'} a_{i\gamma\sigma'} \qquad (8)$$

remains spin-rotationally invariant under a global rotation of the fermion spin $\mathbf{S}_{i\gamma} = \Psi^\dagger_{i\gamma} \frac{\boldsymbol{\sigma}}{2} \Psi_{i\gamma}$ [where $\Psi^\dagger_{i\gamma} \equiv (a^\dagger_{i\gamma\uparrow} a^\dagger_{i\gamma\downarrow})$ is the fermion field operator], even if orbitals γ are identified with the Mn orbitals (t_{2g}, e_g) resulting from crystal-field splitting of the atomic $3d$ orbitals. As the intra-atomic exchange interaction F_0 is much larger than the spin excitation energy scale $(\sim \frac{t^2}{U+F_0}$, within a strong-coupling expansion), all fermion spins on a site are effectively coupled, yielding a composite quantum spin S and a corresponding multiplication by a factor $2S$ yields the effective spin-wave energy scale. Therefore, orbital multiplicity does not change the Goldstone-mode structure, and the spin-dynamics energy scale in the orbital Hubbard model is essentially determined by t and $U_{\text{eff}} = U + F_0$.

As the simplest extension to phenomenologically include spin-space anisotropy while retaining only the relevant energy scales t and U_{eff}, we consider the generalized $\mathcal{N}$-orbital Hubbard model[32]

$$H = -t \sum_{i,\delta,\sigma,\gamma} a^\dagger_{i\sigma\gamma} a_{i+\delta,\sigma\gamma} + \frac{U_1}{\mathcal{N}} \sum_{i\gamma\gamma'} a^\dagger_{i\uparrow\gamma} a_{i\uparrow\gamma} a^\dagger_{i\downarrow\gamma'} a_{i\downarrow\gamma'}$$
$$+ \frac{U_2}{\mathcal{N}} \sum_{i\gamma\gamma'} a^\dagger_{i\uparrow\gamma} a_{i\uparrow\gamma'} a^\dagger_{i\downarrow\gamma'} a_{i\downarrow\gamma} \qquad (9)$$

on a triangular lattice with nearest-neighbor hopping be-

tween sites i and $i+\delta$. Here, γ, γ' refer to the (fictitious) degenerate $\mathcal{N}$ orbitals per site. The factor $\frac{1}{\mathcal{N}}$ is included to render the energy density finite in the $\mathcal{N} \to \infty$ limit. The two correlation terms involve density-density and exchange interactions with respect to the orbital indices. The Hartree-Fock (HF) approximation and RPA are of O(1), whereas quantum fluctuation effects appear at higher order within the inverse-degeneracy expansion and thus $1/\mathcal{N}$, in analogy with $1/S$ for quantum spin systems, plays the role of $\hbar$.

The key feature of spin-rotation symmetry of the generalized Hubbard model is highlighted by writing the two interaction terms as

$$H_{\text{int}} - \frac{U_2}{\mathcal{N}} \sum_i \mathbf{S}_i \cdot \mathbf{S}_i + \frac{U_2 - U_1}{\mathcal{N}} \sum_i S_{iz}^2 \qquad (10)$$

in terms of the total spin operator

$$\mathbf{S}_i = \sum_\gamma \psi^\dagger_{i\gamma} \frac{\boldsymbol{\sigma}}{2} \psi_{i\gamma} \equiv \sum_\gamma \frac{\boldsymbol{\sigma}_{i\gamma}}{2}. \qquad (11)$$

An Ising (uniaxial) anisotropy is obtained for $U_1 > U_2$, a planar (XY) anisotropy for $U_2 > U_1$, and full spin-rotation symmetry for $U_1 = U_2$.

In view of the observed anisotropy gaps for both in-plane and out-of-plane excitations in YMnO$_3$, we consider the following fully anisotropic interaction term:

$$H_{\text{int}} = -\frac{U_{x'}}{\mathcal{N}} \sum_i (S_i^{x'})^2 - \frac{U_{y'}}{\mathcal{N}} \sum_i (S_i^{y'})^2 - \frac{U_{z'}}{\mathcal{N}} \sum_i (S_i^{z'})^2. \qquad (12)$$

Here, x', y', and z' refer to the local spin coordinate axes obtained by rotating the fermion spins in the ordering plane by multiples of $120°$ so that the spin ordering direction is identical for all three sublattices. As appropriate for YMnO$_3$, we consider the case $U_{x'} > U_{y'} > U_{z'}$, corresponding to preferential ordering along the easy-axis x' due to the uniaxial anisotropy $U_{x'} - U_{y'}$, similar to the in-plane, easy-axis anisotropy considered within the Heisenberg picture in recent studies.[16] It has been suggested that this anisotropy owes its origin to local distortions around Mn^{3+}.

At the HF level, the interaction term for orbital γ then reduces to

$$H_{\text{int}}^\gamma = -\sum_i \boldsymbol{\sigma}_{i\gamma} \cdot \boldsymbol{\Delta}_i, \qquad (13)$$

where the self-consistently determined mean field $\boldsymbol{\Delta}_i = (U_{x'}) \times \langle \mathbf{S}_i \rangle_{x'}$ lies along the easy-axis direction x'. The HF sublattice magnetization depends only on $U_{x'}$ and is determined from the self-consistency condition $\langle \mathbf{S}_\alpha \rangle_{\text{HF}} = \sum_{\mathbf{k},l} \langle \mathbf{k}, l | \frac{\boldsymbol{\sigma}}{2} | \mathbf{k}, l \rangle_\alpha$ in terms of the HF states $|\mathbf{k},l\rangle$ on sublattice α, exactly as for the isotropic case.[25] In the strong-coupling limit, the sublattice magnetization $\langle \mathbf{S}_\alpha \rangle \approx 1/2$ at the HF level, and is reduced by about $(1/2S)50\%$ (in the isotropic case and for spin quantum number S) due to quantum fluctuations of order $1/2S$, as found in different calculations cited in Ref. 9.

We consider the 120° ordered AF state on the triangular lattice and examine transverse spin fluctuations about the broken-symmetry state. Introducing the above-mentioned spin-rotation transformation, we obtain for the transverse spin-fluctuation propagator

$$[\chi(\mathbf{q},\omega)]_{\alpha\beta}^{\mu\nu} = \frac{[\chi^0(\mathbf{q},\omega)]}{\mathbf{1} - 2[U][\chi^0(\mathbf{q},\omega)]} \quad (14)$$

in the $2 \otimes 3$ spin-sublattice basis of the two transverse spin directions μ, $\nu = y', z'$ and the three sublattices α, $\beta = A, B, C$. The sublattice-diagonal interaction matrix

$$[U] = \begin{bmatrix} U_{y'}\mathbf{1} & \mathbf{0} \\ \mathbf{0} & U_{z'}\mathbf{1} \end{bmatrix} \quad (15)$$

in the y', z' basis and the bare particle-hole propagator

$$[\chi^0(\mathbf{q},\omega)]_{\alpha\beta}^{\mu\nu} = \frac{1}{4} \sum_{\mathbf{k},l,m} \frac{\langle\sigma_\mu\rangle_\alpha^{-+}\langle\sigma_\nu\rangle_\beta^{-+*}}{E_{\mathbf{k}-\mathbf{q},m}^+ - E_{\mathbf{k},l}^- + \omega} + \frac{\langle\sigma_\mu\rangle_\alpha^{+-}\langle\sigma_\nu\rangle_\beta^{+-*}}{E_{\mathbf{k},m}^+ - E_{\mathbf{k}-\mathbf{q},l}^- - \omega} \quad (16)$$

involve integrating out the fermions in the broken-symmetry state. In the particle-hole matrix elements of the rotated spins

$$\langle\sigma_\mu\rangle_\alpha^{-+} \equiv \langle\mathbf{k}-\mathbf{q},m|\sigma_\mu|\mathbf{k},l\rangle_\alpha \quad (17)$$

the spin orientation angles ϕ_α in the fermion states are transformed out. The numerical evaluation of $[\chi^0(\mathbf{q},\omega)]$ in terms of the HF-level AF-state energies and amplitudes is exactly the same as for the isotropic case studied earlier.[25]

The spin-wave energies $\omega_\mathbf{q}$ are then obtained from the poles $1 - \lambda_\mathbf{q}(\omega_\mathbf{q}) = 0$ of Eq. (16) in terms of the eigenvalues $\lambda_\mathbf{q}(\omega)$ of the $2[U][\chi^0(\mathbf{q},\omega)]$ matrix. As $\omega_\mathbf{q}$ obtained for the Hubbard model corresponds to spin 1/2, the spin-wave energy is scaled by the factor $2S$ for arbitrary spin S.[33] As expected from the in-plane easy-axis anisotropy $U_{x'} - U_{y'}$ and out-of-plane anisotropy $U_{x'} - U_{z'}$, all three Goldstone modes, corresponding to uniform ($q=0$) twisting of spins away from the ordering direction, become massive. The observed magnitudes of the in-plane and out-of-plane anisotropy gaps are $\omega_{gap}^{y'} \simeq 2.5$ meV and $\omega_{gap}^{z'} \simeq 5$ meV, respectively.

Figure 16 shows the spin-wave dispersion for the three modes along a symmetry direction in the MBZ, along with the neutron-scattering data for YMnO₃ in the low-temperature ordered phase. The anisotropic Hubbard model provides a remarkably good description of the spin dynamics. Best fits are obtained only in the strong-coupling limit ($U/t > \sim 15$), with planar exchange energy $J = 4t^2/U \simeq 2.4$ meV and anisotropy terms $D_z = U_{x'} - U_{z'} \simeq 0.32$ meV and $D_y = U_{x'} - U_{y'} \simeq 0.033$ meV. These values of exchange energy J and the out-of-plane anisotropy term D_z are very close to those obtained from the HoMnO₃ data,[24] suggesting an intrinsic Mn-spin origin.

In order to highlight the finite-U, double-occupancy effect in the triangular-lattice antiferromagnet, we also show the spin-wave dispersion evaluated for somewhat smaller interaction strength ($U/t \approx 9$), which is comparable to the bandwidth. Figure 17 shows noticeable relative softening of mode
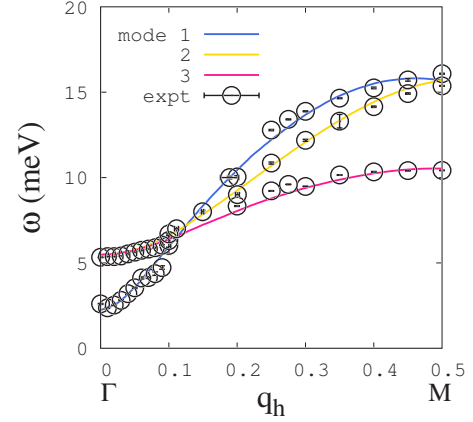

FIG. 16. (Color online) Spin-wave dispersion for the three modes calculated for the anisotropic Hubbard model with planar exchange energy $J = 4t^2/U \simeq 2.4$ meV, $D_z = U_{x'} - U_{z'} \simeq 0.32$ meV, and $D_y = U_{x'} - U_{y'} \simeq 0.033$ meV, along with neutron-scattering data points for YMnO₃ in the low-temperature ordered phase.

3 as well as enhanced separation between modes 1 and 2, which provide sensitive indicators of finite-U effects.

We have recently evaluated the magnon energies in the strong-coupling limit ($U/t \gg 1$) in order to make contact with the Heisenberg model result. Evaluating $[\chi^0(\mathbf{q},\omega)]$ by expanding the AF-state energies $E_\mathbf{k}$ and the particle-hole matrix elements up to order t^2/U^3, we obtain for the magnon energy[34]

$$\omega_\mathbf{q} = 3JS\left[\left(1 - \gamma_\mathbf{q} + \frac{2D_y}{3J}\right)\left(1 + 2\gamma_\mathbf{q} + \frac{2D_z}{3J}\right)\right]^{1/2}, \quad (18)$$

where

$$\gamma_\mathbf{q} = \frac{1}{3}\left(\cos q_x + 2\cos\frac{q_x}{2}\cos\frac{\sqrt{3}q_y}{2}\right). \quad (19)$$

The three magnon branches correspond to momentum values $\mathbf{q}$ and $\mathbf{q}\pm\mathbf{Q}$, where $\mathbf{Q} = (2\pi/3, 2\pi/\sqrt{3})$ is the ordering wave vector and $\mathbf{q}$ lies inside the MBZ.
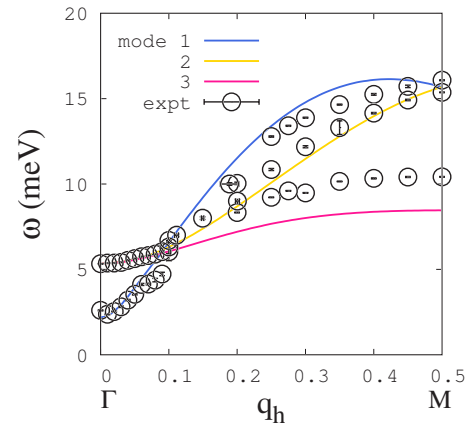

FIG. 17. (Color online) Noticeable relative softening of mode 3, which is a characteristic finite-U, double-occupancy effect in the triangular-lattice antiferromagnet, seen in the spin-wave dispersion evaluated for $U/t \approx 9$.

At the zone center $\mathbf{q}=0$, the three branches correspond to momenta values 0 and $\pm\mathbf{Q}$ with $\gamma_\mathbf{q}=1$ and $-1/2$, respectively. Correspondingly, we obtain magnon energies $3JS[(2D_y/3J)(3)]^{1/2}$ and $3JS[(2D_z/3J)(3/2)]^{1/2}$, representing anisotropy gaps for in-plane and out-of-plane spin twistings. The ratio $\sqrt{2}(D_y/D_z)^{1/2}$ of these two anisotropy gaps directly relates the ratio of the anisotropy parameters D_y/D_z to the ratio of the observed anisotropy gaps (~ 2.5 meV/5 meV).

VIII. SUMMARY

We have investigated the antiferromagnetic phase transition of the quasi-2D YMnO$_3$ by studying the temperature variation of the magnetic Bragg reflection and temperature dependence of the rodlike diffuse magnetic scattering across the phase transition temperature $T_N \approx 70$ K. The critical exponents β, γ, and ν have been determined and compared with the theoretical values. We have investigated the spin dynamics of YMnO$_3$ by inelastic neutron scattering and determined the spin-wave dispersion at low temperature. The spin-wave dispersions at low temperature have been analyzed with a simple nearest-neighbor anisotropic Heisenberg model and also by an anisotropic Hubbard model. We have shown that in the strong-coupling limit, the anisotropic Hubbard model maps into the anisotropic Heisenberg model. The characteristic relative softening of mode 3 due to finite-U frustration effects is not observed in the neutron-scattering data, confirming the strong-coupling limit as appropriate.

ACKNOWLEDGMENTS

[1] *Colossal Magnetoresistive Oxides*, edited by Y. Tokura (Gordon and Breach, New York, 2000).

[2] *Colossal Magnetoresistive Manganites*, edited by T. Chatterji (Kluwer Academic, Dordrecht, 2004).

[3] Z. J. Huang, Y. Cao, Y. Y. Sun, Y. Y. Xue, and C. W. Chu, Phys. Rev. B **56**, 2623 (1997).

[4] E. F. Bertaut and M. Mercier, Phys. Lett. **5**, 27 (1963).

[5] W. C. Koehler, H. L. Yakel, E. O. Wollan, and J. W. Cable, Phys. Lett. **9**, 93 (1964).

[6] D. G. Tomuta, S. Ramkrishnan, G. J. Nieuwenhuys, and J. A. Mydosh, J. Phys.: Condens. Matter **13**, 4543 (2001).

[7] T. Katsufuji, S. Mori, M. Masaki, Y. Moritomo, N. Yamamoto, and H. Takagi, Phys. Rev. B **64**, 104419 (2001).

[8] A. Munoz, J. A. Alonso, M. J. Martínez-Lope, M. T. Casáis, J. L. Martínez, and M. T. Fernández-Díaz, Phys. Rev. B **62**, 9498 (2000).

[9] T. Lonkai, D. Hohlwein, J. Ihringer, and W. Prandl, Appl. Phys. A: Mater. Sci. Process. **74**, 5843 (2002).

[10] D. Fröhlich, St. Leute, V. V. Pavlov, and R. V. Pisarev, Phys. Rev. Lett. **81**, 3239 (1998).

[11] M. Fiebig, D. Fröhlich, K. Kohn, St. Leute, Th. Lottermoser, V. V. Pavlov, and R. V. Pisarev, Phys. Rev. Lett. **84**, 5620 (2000).

[12] A. V. Kimel, R. V. Pisarev, F. Bentivegna, and Th. Rasing, Phys. Rev. B **64**, 201103(R) (2001).

[13] G. E. Bacon, *Neutron Diffraction* (Clarendon, Oxford, 1975).

[14] P. J. Brown and T. Chatterji, J. Phys.: Condens. Matter **18**, 10085 (2006).

[15] Th. Jolicoeur and J. C. Le Guillou, Phys. Rev. B **40**, 2727 (1989).

[16] T. J. Sato, S.-H. Lee, T. Katsufuji, M. Masaki, S. Park, J. R. D. Copley, and H. Takagi, Phys. Rev. B **68**, 014432 (2003).

[17] J. Park, J.-G. Park, G. S. Jeon, H.-Y. Choi, C. Lee, W. Jo, R. Bewley, K. A. McEwen, and T. G. Perring, Phys. Rev. B **68**, 104426 (2003).

[18] M. F. Collins, *Magnetic Critical Scattering* (Oxford University Press, Oxford, 1989).

[19] R. A. Cowley, in *Neutron Scattering*, edited by K. Sköld and D. L. Price, Methods of Experimental Physics Vol. 23 (Academic, Orlando, 1987), Pt. C.

[20] B. Roessli, S. N. Gvasaliya, E. Pomjakushina, and K. Conder, JETP Lett. **81**, 360 (2005).

[21] T. Lonkai, D. G. Tomuta, J.-U. Hoffmann, R. Schneider, D. Hohlwein, and J. Ihringer, J. Appl. Phys. **93**, 8191 (2003).

[22] F. Demmel and T. Chatterji, Phys. Rev. B (to be published).

[23] O. P. Vajk, M. Kenzelmann, J. W. Lynn, S. B. Kim, and S.-W. Cheong, Phys. Rev. Lett. **94**, 087601 (2005).

[24] Pramana, J. Phys. (to be published).

[25] A. Singh, Phys. Rev. B **71**, 214406 (2005).

[26] R. Coldea, S. M. Hayden, G. Aeppli, T. G. Perring, C. D. Frost, T. E. Mason, S.-W. Cheong, and Z. Fisk, Phys. Rev. Lett. **86**, 5377 (2001).

[27] A. Singh and P. Goswami, Phys. Rev. B **66**, 092402 (2002).

[28] R. Sachidanandam, T. Yildirim, A. B. Harris, A. Aharony, and O. Entin-Wohlman, Phys. Rev. B **56**, 260 (1997).

[29] E. Hanamura, K. Hagita, and Y. Tanabe, J. Phys.: Condens. Matter **15**, L103 (2003).

[30] L. M. Roth, Phys. Rev. **149**, 306 (1966).

[31] K. Held and D. Vollhardt, Eur. Phys. J. B **5**, 473 (1998).

[32] A. Singh, Phys. Rev. B **43**, 3617 (1991).

[33] A. Singh and P. Sen, Phys. Rev. B **57**, 10598 (1998).

[34] S. Ghosh and A. Singh (unpublished).